Available online at www.sciencedirect.com
SCIENCE DIRECT
Solid State Ionics 170 (2004) 239–254
SOLID STATE IONICS
www.elsevier.com/locate/ssi

Ionic and electronic conductivity in lead–zirconate–titanate (PZT)

Bernard A. Boukamp*, Mai T.N. Pham, Dave H.A. Blank, Henny J.M. Bouwmeester

Inorganic Materials Science, Faculty of Science and Technology and MESA+ Institute for Nanotechnology, University of Twente, P.O. Box 217, Enschede 7500 AE, The Netherlands

Received 15 December 2003; received in revised form 4 March 2004; accepted 4 March 2004

Abstract

Accurate impedance measurements on differently sized samples of lead–zirconate–titanate ($PbZr_{0.53}Ti_{0.47}O_3$, PZT) have been analyzed with a CNLS procedure, resulting in the separation of the ionic and electronic conductivities over a temperature range from ~ 150 to 630 °C. At 603 °C the electronic conductivity shows approximately a $(P_{O_2})^{1/4}$ dependence, while the ionic conductivity remains constant. Below the Curie transition temperature the oxygen non-stoichiometry becomes frozen-in and the conductivities are strongly dependent on the sample history with respect to temperature sequence and ambient P_{O_2}. A tentative interpretation assumes defect association, i.e. formation of neutral $[V''_{Pb}-V^{\bullet\bullet}_O]\times$ complexes, and electron-hole transfer between lead sites and lead vacancies to control the oxygen ion conductivity in the tetragonal phase.

Annealing PZT-based devices at about 600 °C under low oxygen pressure (~ 1 Pa oxygen) effectively decreases the low temperature electronic conductivity by a factor of 100 and the ionic conductivity by a factor of 10–15 with respect to normal air processing.

PACS: 66.10.Ed; 66.30.Hs; 72.20.+*i*; 72.60.+*g*; 84.37
Keywords: PZT; Mixed electronic ionic conductor (MIEC); Diffusion; Ferroelectric material; Impedance analysis

1. Introduction

Lead–zirconate–titanate ($PbZr_{0.53}Ti_{0.47}O_3$, short: PZT) is a well-known ferro-electric material with a high dielectric constant, high polarization and low coercive field [1]. It has potential for application as capacitor material or in thin film memory devices. It was recently found that introduction of a well dispersed highly conducting second phase (e.g. Pt) in PZT can lead to a significant enhancement in the dielectric constant [2,3].

At room temperature PZT is an almost pure dielectric material with a (total) conductivity of less than 10^{-15} S cm^{-1}. Above about 150 °C the conductivity becomes appreciable, but there still exists some doubt about the type of conductivity. For quenched samples Raymond and Smyth [4] suggested a predominantly ionic conductivity at low temperatures. They considered the lead centers to act as deep traps for electron holes:

$$h^{\bullet} + Pb^{\times}_{Pb} \rightleftarrows Pb^{\bullet}_{Pb} \quad (1)$$

resulting in a high activation energy for the electronic conduction. In this publication the well-known Kröger-Vink notation for crystal defects is used. Prisedsky et al. [5] studied the conductivity and Seebeck coefficient of PZT between 600 and 1000 °C as function of P_{O_2}. The PbO partial pressure was controlled by either a two-phase mixture of PZT and PbO (PbO-rich) or PZT and ZrO_2 (PbO-poor). Their main conclusions were that lead and oxygen vacancies formed the majority defects. In the P_{O_2} range from 10 to 100 kPa the electro-neutrality condition would be presented by:

$$2[V''_{Pb}] = 2[V^{\bullet\bullet}_O] + h^{\bullet} \quad (2)$$

with $[V^{\bullet\bullet}_O] \gg h^{\bullet}$. The *p*-type electronic conductivity showed a $(P_{O_2})^{1/4}$ dependence and was assigned to small polaron hopping. Leveling off of the $\log\sigma - \log P_{O_2}$ plot at the low P_{O_2} side indicated ionic conductivity. Nonaka et al. [6] studied the influence of Pb-deficiency on the photovoltaic

* Corresponding author. Tel.: +31-53-4892990; fax: +31-53-4894683.
E-mail address: b.a.boukamp@utwente.nl (B.A. Boukamp).
URL: http://www.ims.tnw.utwente.nl.

0167-2738/$ - see front matter © 2004 Elsevier B.V. All rights reserved.
doi:10.1016/j.ssi.2004.03.005

properties and on the electronic conductivity of PZT (with Zr/Ti molar ratio 0.5/0.5). A strong increase in the conductivity was observed when the Pb/(Zr+Ti) molar ratio fell below 1.

Few impedance studies have been performed on PZT and related compositions. Las et al. [7] have studied the influence of the calcining and sintering temperatures on the electrical properties of PZT. The impedance spectra were interpreted in terms of electronic conduction hindered by a grain boundary effect. Peláiz Barranco et al. [8] investigated lanthanum doped PZT using impedance spectroscopy. The CNLS-analysis, however, did not yield a clear separation between ionic and electronic conductivity. They also studied the complex PZT-$PbCuNbO_3$ system [9], but here the frequency dispersion was analyzed with a simple (*RC*) circuit, which showed a rather poor match with the experimental dispersion.

In order to understand the conductive processes in the dual phase PZT/Pt compounds [2,3] knowledge of the conduction and, hence, of the defect chemistry in pure PZT is essential. Therefore we performed an impedance study of the conductivity of PZT in the temperature range from 20 to 650 °C and as function of P_{O_2} at selected temperatures.

2. Experimental procedure

2.1. Sample preparation

The samples were prepared from commercial PZT powder (TRS Ceramics, State College, PA, USA) with a Zr/Ti ratio of 53:47. The composition of the starting powder was analyzed with Röntgen fluorescence analysis (XRF, Philips PW 1480). The powder was pressed into pellets with a diameter of 10 mm, first by uniaxial pressing, followed by isostatic pressing at 4000 MPa. The samples were sintered in air at 1150 °C for 2 h. The samples were embedded in $PbTiO_3$ powder in a closed Pt crucible in order to minimize loss of Pb during sintering. The phase purity of the samples was checked with XRD (Philips X'Pert APD). Afterwards the samples were cut to size (cylinders of about 8.0 mm diameter and with a thickness between 1 and 3 mm). The flat surfaces were polished with diamond paste.

Extensive measurements were performed on two samples with different thickness. A thick sample, noted further on as 'large' or [L] which was 2.95 mm thick, and a thin sample, noted further on as 'small' or [S] which was 1.0 mm thick. Both samples had a diameter of 8.05 mm. The density of all samples was 98–99% of the theoretical density. The average grain size was in the range 5–10 μm.

2.2. Impedance measurements

In order to be able to distinguish between the ionic and electronic contributions to the total conduction, dense thin gold electrodes were deposited on both sides of the samples by dc-sputtering. As it was observed that the thin sputtered electrodes were not stable at 500–600 °C, the thermal stability, and hence the lateral conduction, of the gold electrodes was improved by applying additional gold paint layers, which were cured at 700 °C. Comparison with samples with only sputtered electrodes indicated that the 700 °C cure had no effect on the properties. In previous studies [10–12] it has been shown that gold has little activity towards oxygen dissociation, and hence behaves as a more or less blocking electrode for the ionic conduction path. The use of two samples with identical cross section but different thickness can allow distinction between bulk and interface responses [12]. In the conductivity cell, both samples were placed adjacent to each other between gold electrodes, sharing a central gold electrode. This ensured that measurements on both samples were carried out at identical temperature and ambient.

The oxygen partial pressure was regulated between 1 Pa ($\sim 10^{-5}$ atm) and 75 kPa (0.75 atm) using two gas-flow controllers. Nitrogen was used as balance gas. The actual oxygen partial pressure was measured directly at the vent of the conductivity cell with an oxygen sensor (Systech, model ZR 893/4). For most measurements an 80/20 N_2/O_2 mixture was used.

Impedance data were collected in the frequency range 0.1 Hz to 65 kHz using a frequency response analyzer (Solartron 1250) in combination with high impedance differential preamplifiers. After each temperature or P_{O_2} change, the samples were allowed to equilibrate for a substantial amount of time. An amplitude of 50 mV (rms) was used. The impedance data were validated using a specially developed Kramers-Kronig test program [13] and subsequently analyzed with the CNLS-fit program 'Equivalent Circuit' [14,15].

2.3. Measurement sequence

The two samples (large and small) were slowly heated in a 80/20 N_2:O_2 gas stream to 603 °C. At this temperature the P_{O_2} dependence of the impedance was measured. Next the impedances were measured as function of temperature down to 200 °C in the same gas mixture. In order to allow the samples to equilibrate with the ambient a waiting time of minimal 3- to 4 h was observed before the next set of impedance spectra was acquired.

Next, spectra were measured up to 360 °C, again in a 80:20 N_2/O_2 flow. At 360 °C the apparent P_{O_2} dependence was surveyed. The P_{O_2} was stepped from 20 kPa (~ 0.2 atm) down to 1 Pa (10^{-5} atm) by passing only nitrogen. Impedances were measured as function of time over a period of 2 weeks. Two steps with increasing P_{O_2} were executed while the time dependences of the impedances were recorded.

Subsequently, the temperature was slowly increased to 603 °C and a few P_{O_2} dependencies were recorded down to a P_{O_2} of ~ 1 Pa (nitrogen flow). At this point the samples were rapidly cooled down to room temperature by placing the measurement cell outside of the furnace. Finally the

impedances were recorded as a function of temperature in a P_{O_2} of $\sim$ 1 Pa, using a nitrogen gas flow.

3. Results

3.1. Sample purity

The XRF analysis showed for the starting powder a composition of $Pb_{0.98}Zr_{0.53}Ti_{0.47}O_3$. Hafnium was found as the major impurity (0.4 wt.% HfO_2). Hafnium is a normal companion of zirconium and is generally assumed to have the same properties as zirconium in most compositions. A small amount of iron was also detected, about 2×10^{-3} wt.% Fe_2O_3. Al, Mg, Na and Si were not found, but the limit of detection is rather insensitive (respectively 0.13, 0.25, 0.4 and 0.1 wt.%, based on the oxides). XRD-analysis at room temperature showed for the sintered samples only peaks of tetragonal PZT.

4. Data analysis

The impedance spectra measured in air showed generally a large, somewhat depressed semicircle with a clear dc point representing the electronic resistance, R_{el}. Depending on temperature and P_{O_2} an extra semicircle contribution becomes visible at low frequencies. A series of frequency dispersions for both large and small sample is presented in the impedance representation in Fig. 1. The data, which have been measured from 603 °C down to room temperature, have been corrected for sample dimensions. Below about 150 °C the dispersion becomes capacitive in nature, it is no longer possible to extract the dc-resistance with acceptable accuracy from the measured dispersions.

The CNLS-fit analysis of the high temperature data for P_{O_2} values above 1 kPa resulted in a simple equivalent circuit: a parallel combination of the dielectric CPE response, Q_{diel}, the electronic resistance, R_{el}, and the blocked ionic path presented by R_{ion} and a CPE, resulting in a simple circuit description code or CDC [15]: $(Q_{diel}R_{el}[R_{ion}Q_{block}])$[1]. The schematic equivalent circuit is presented in Fig. 2A. The other measurements required a more complex equivalent circuit, in many instances the circuit of Fig. 2B gave an excellent match to the data. In this case an extra (RQ) circuit, which is tentatively assigned to grain boundary dispersion, was included in the ionic path, CDC: $(Q_{diel}R_{el}[R_{ion}(R_{gb}Q_{gb})Q_{block}])$.

In a number of cases (especially in N_2 atmosphere) the assumed interface dispersion needed to be modeled with a Randles type circuit, as indicated by Fig. 2C. Despite the complexity of this equivalent circuit, the parameters obtained with it showed, as function of temperature, a clear trend with little scatter. Fig. 3 presents the deconvolution of such a typical data set. Fig. 3A shows the measured impedance together with the CNLS-fit, the insert represents the relative residuals of the fit [13,14]. After subtraction of the dielectric dispersion, Q_{diel}, and the electronic resistance, R_{el}, the entire ionic path is revealed in Fig. 3B. Here the insert magnifies the high frequency region, indicating another dispersion. Subsequent subtraction of the electrode response (Randles circuit) leaves the bulk ionic contribution, Fig. 3C, tentatively interpreted with $R_{ion}(R_{gb}Q_{gb})$. Isolating the electrode response and subtracting the parallel double layer capacitance, C_{dl}, clearly reveals the Warburg contribution and the charge transfer resistance in Fig. 3D. For clarity the parameters obtained from the overall CNLS-analysis have been used in the subtraction processes. These parameter values and error estimates are presented in Table 1. It is quite remarkable that with this complex circuit (Fig. 2C) and the rather featureless dispersion of Fig. 3A such low error estimates are obtained. The full interpretation of the CNLS-analysis will be presented in the discussion section.

4.1. Dielectric constant

The phase transformation from low temperature tetragonal to cubic above the Curie transition is marked by a large peak in the dielectric constant. At temperatures below $\sim$ 150 °C the dielectric response is purely capacitive, but with increasing temperature the CNLS-analysis yields a CPE type response:

$$Y(\omega) = Y_0(j\omega)^n \tag{3}$$

with the frequency power, n, steadily decreasing from almost 1 at room temperature to about $n = 0.7-0.8$ above T_C. Calculating ε_{real} from Eq. (3) yields considerable scatter in the $\varepsilon_{real}-T$ plot. A much better approach is including the frequency exponent in the pre-factor Y_0:

$$\varepsilon_{real} = \frac{Y_0^{1/n} \cdot d}{A \cdot \varepsilon_0} \tag{4}$$

Using this equation a clear peak in the dielectric response around the Curie point at 400 °C is observed, see Fig. 4. The dielectric response was found to be independent of the oxidation state of the samples. An identical response is observed in N_2 ambient (open symbols at 1.1 Pa oxygen). Using expression (4) for the dielectric constant the Curie–Weiss law is obeyed over a temperature range from 400 to $\sim$ 520 °C, as is demonstrated with the ε^{-1} versus T plot shown as insert in Fig. 4. It should be noted, however, that a more complex theory might be needed to model the Curie peak [16]. The Curie constant, estimated from Fig. 4 (insert) is with $1-2 \times 10^5$ in the proper range.

[1] In addition to the circuit description code presented in Ref. [15], the square brackets indicate a series arrangement, the parenthesis only a parallel arrangement.

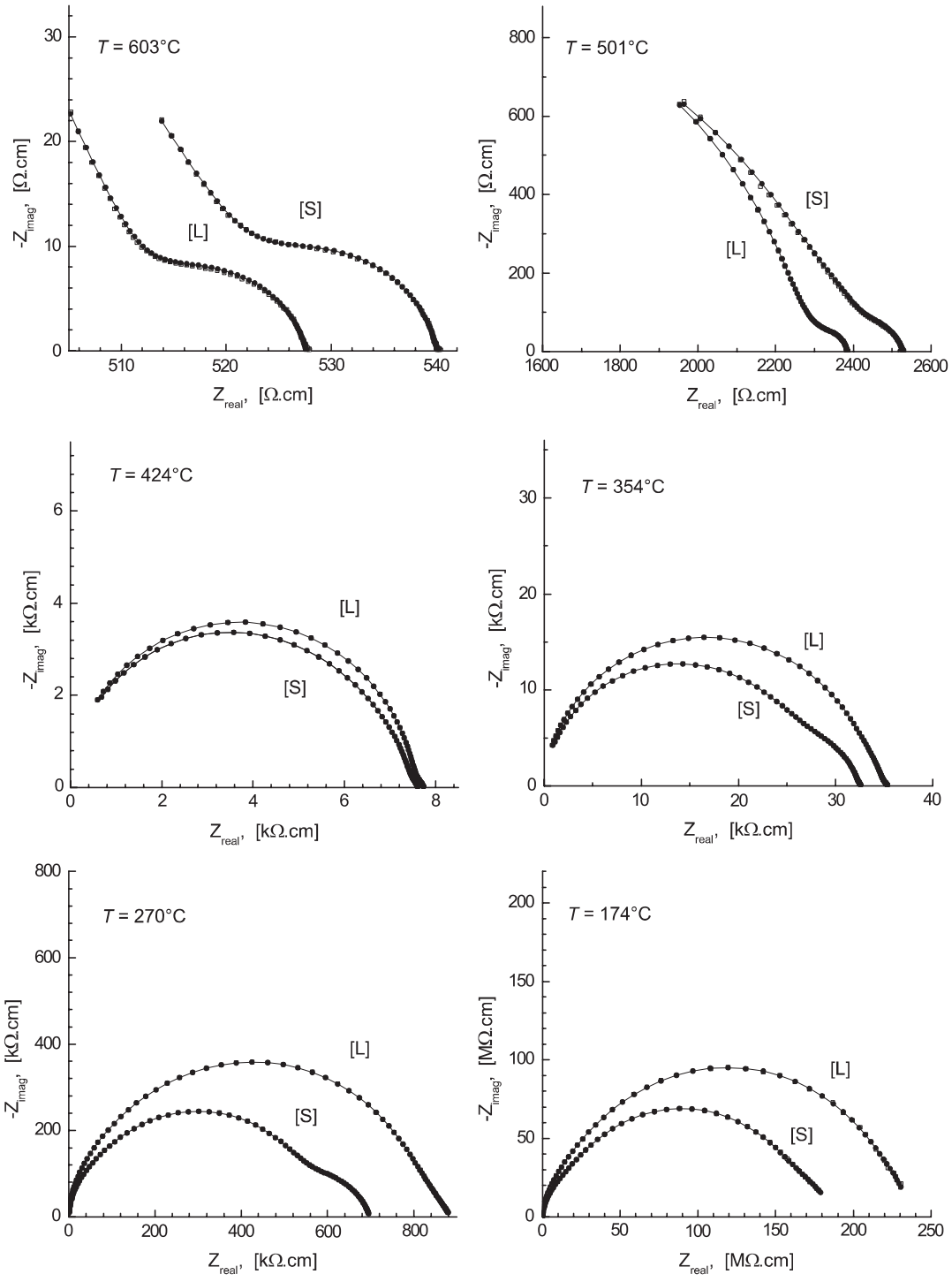

Fig. 1. Change of the frequency dispersion of the large [L] and small [S] sample with temperature, measured from 603 °C down to 174 °C. Data is scaled for sample dimensions. Continuous line represents the CNLS-fit. Frequency range: 0.1–65 kHz, ambient $N_2/O_2 = 80/20$, $P_{O_2} = 20$ kPa.

4.2. High temperature conductivity and P_{O_2} dependence

After slow heating of the samples to ~600 °C in a 80/20 N_2/O_2 gas mixture, the impedances were measured as function of P_{O_2} between ~75 kPa and ~1 Pa. Sufficient time was allowed for equilibration after each change in the P_{O_2}. Equilibrium conditions were checked with the Kramers-Kronig test software [13]. After a small step in the P_{O_2} about 3–4 h was generally found to be sufficient for equilibration at this temperature. The electronic conductivity (obtained from the 'dc-point') showed a clear $P_{O_2}^{1/4}$ dependence, indicating *p*-type conductivity. The total ionic conductivity (combination of R_{ion} and R_{gb}) remained constant within the experimental error. A very

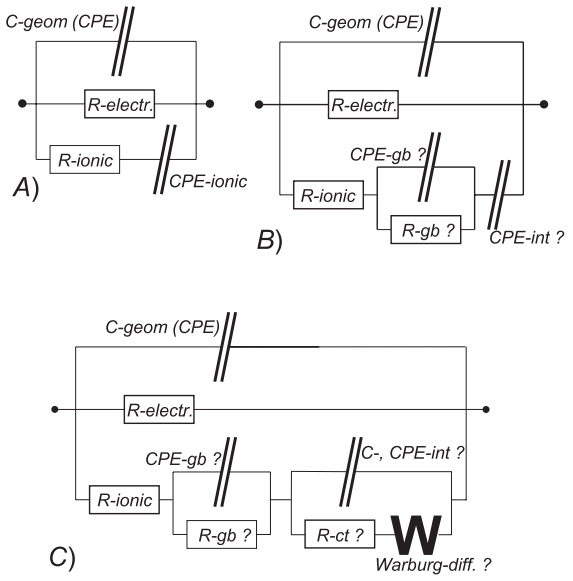

Fig. 2. Equivalent circuits used in the analysis of the impedance data, for explanation see text.

good match was observed for the conductivities of the small and large sample, as can be seen in Fig. 5.

4.3. Electronic conductivity in air

Fig. 6 shows the temperature dependence of the electronic conductivity. Clearly two different regions with activated behavior can be discerned, in accordance with literature. Above the Curie point the activation energy is 83 kJ·mol^{-1} (0.74 eV). A transition region to low temperature-activated behavior coincides with the width of the Curie peak in the dielectric constant (see Fig. 6). It is remarkable that there is a small but constant difference between the electronic conductivity of the small and the large sample in the low temperature region. The difference is about a factor 1.25 and is caused by a difference in the oxygen non-stoichiometry of the samples. At high temperature the samples are in thermodynamic equilibrium with the ambient. On cooling down this equilibration process becomes sluggish and, hence, is strongly influenced by the sample dimensions. The conductivity of the large sample

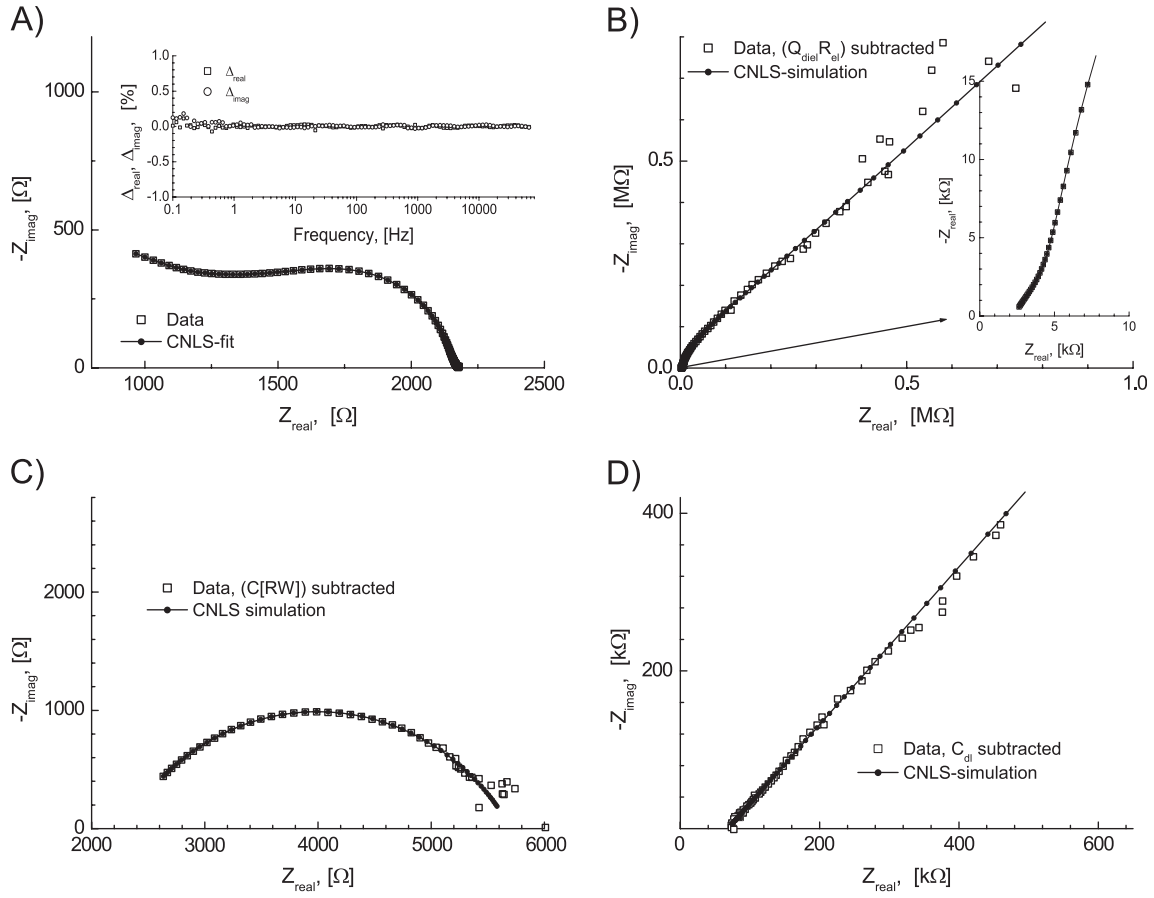

Fig. 3. Example of deconvolution of data according to the equivalent circuit of Fig. 2C. Dispersion of small sample at 580 °C in N_2 (P_{O_2} = 1.1 Pa), frequency range 0.1 Hz–65 kHz. (A) Impedance spectrum with CNLS-fit, insert shows the relative residuals. (B) Dispersion after parallel subtraction of Q_{diel} and R_{el}, insert shows magnification of high frequency range. (C) 'Ionic path', revealed after subtraction of interface (Randles) dispersion. (D) Warburg and R_{ct} after subtraction of C_{dl} from the interface dispersion (ionic path has also been subtracted from dispersion of B).

Table 1
CNLS-fit results of the analysis of the dispersion presented in Fig. 3, small sample in N_2 at 580 °C

CDC	($Q_1R_2[R_3(R_4Q_5)(C_6[R_7W_8])]$)			
	Kramers-Kronig test		CNLS-analysis	
Pseudo χ^2	5.8×10^{-8}		2.0×10^{-7}	
Element	Assignment	Value	Rel.err. (%)	Unit
Q_1-Y_0	dielectric	3.1×10^{-9}	14	[S·s^n]
Q_1-n	response	0.888	1	–
R_2	electronic	2180	0.01	[Ω]
R_3	ionic	2260	3	[Ω]
R_4	grain boundary	3470	3	[Ω]
Q_5-Y_0	grain boundary	3.0×10^{-7}	11	[S·s^n]
Q_5-n	'capacitance'	0.663	1.8	–
C_6	double layer	1.75×10^{-8}	0.9	[F]
R_7	charge transfer	69500	2.8	[Ω]
W_8-Y_0	diffusion	4.32×10^{-7}	2.5	[S·s$^{1/2}$]

relates to a frozen-in equilibrium state from a higher temperature than for the small sample.

4.4. Ionic conductivity in air

The ionic conductivity is far more difficult to extract than the electronic conductivity. Hence more scatter is observed in the ionic conductivity and the connected grain boundary conductivity (see Fig. 2B and C). Both are displayed in the Arrhenius graph of Fig. 7. To facilitate comparison with electronic conductivity (Fig. 6) the ionic conductivity as presented as $\ln\sigma$ vs. T^{-1}, rather than the usual $\ln\sigma T$ vs. T^{-1}. Only for the large sample a clear activated behavior is observed in the high temperature region. Estimation of the ionic conductivity in this region is complicated for the small sample. The grain boundary conductivity shows even more scatter, but still clear trends are visible in Fig. 7. High temperature Arrhenius behavior of the ionic conductivity of the large sample extends almost to the low temperature onset of the Curie peak in ε, followed by a rapid transition to a higher value at a somewhat lower temperature. For the small sample the changeover is more gradual, but both conductivities show Arrhenius type behavior in the low temperature regime. Again the values for the small sample are shifted with respect to large sample. The activation energy is close to that for the electronic conductivity in this temperature range, see Table 2.

The grain boundary conductivity seems to follow the slope of the ionic conductivity, but is about a factor 5 smaller in the low temperature region. The values appear closer above the Curie transition. Despite the complexity in extracting the ionic conductivities with the CNLS-procedure, identical values and temperature dependencies are obtained for both samples, thus adding to the credibility of the followed analysis procedure and choice of equivalent circuits.

4.5. P_{O_2} dependence below the Curie temperature

After completing the conductivity measurements in air the P_{O_2} dependence at 360 °C, well below the Curie transition, was measured. Earlier measurements on identical samples indicated a P_{O_2} dependence of ~ 0.11 for both the electronic and ionic conductivity. These measurements were carried out from 20 kPa down to 100 Pa in a few steps, with waiting times of 3–4 h after each P_{O_2}-step. The measurements were not really reproducible upon increasing the P_{O_2}, clearly indicating that equilibration with the ambient was still continuing at this temperature, but at a very slow rate.

Hence in this experiment with two samples the P_{O_2} was stepped from 20 kPa to ~ 1 Pa at 360 °C and the

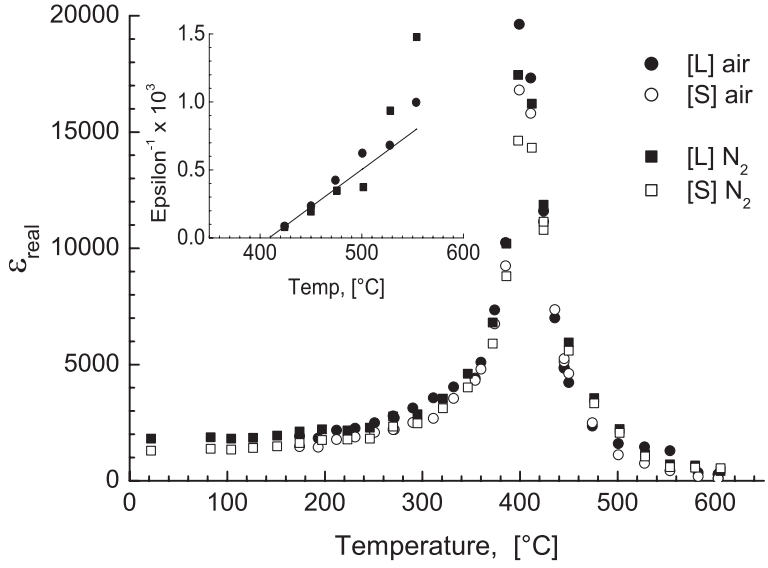

Fig. 4. Real part of the dielectric constant, ε_{real}, as function of temperature for the large (closed symbols) and small (open symbols) sample. Ambient, air: circles; N_2 ($P_{O_2} \sim 1.1$ Pa) squares. The dielectric constant is calculated according to Eq. (4). The insert show the Curie–Weiss law behaviour for the thick sample.

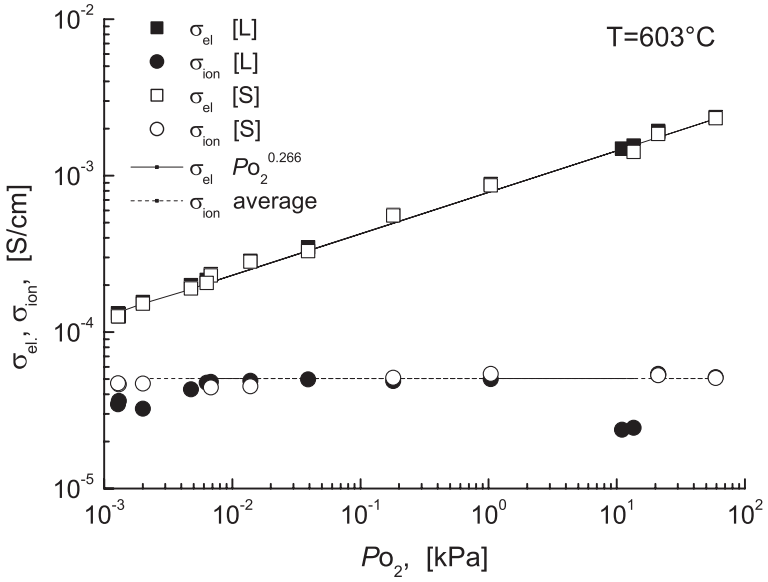

Fig. 5. P_{O_2} dependence of the electronic (■,□) and ionic (●,○) conductivity at 602 °C. Closed symbols: large sample, open symbols: small sample. Lines present fits to the data points (excluding obvious outliers).

impedances were measured over two weeks time. The small sample showed a faster response to the change in P_{O_2} than the large sample. The change in electronic resistance in time is depicted in Fig. 8. Here the response is treated in terms of the well-known experimental conductivity relaxation approach [17,18] and is presented as a normalized dimensionless electronic conductivity:

$$\overline{\sigma(t)} = \frac{\sigma(t) - \sigma_0}{\sigma_\infty - \sigma_0} \tag{5}$$

where σ_0 is the value of σ_{el} at $t=0$ and σ_∞ at $t=\infty$. The response of the large sample was modeled with a diffusion-limited response, i.e. the surface transfer reaction is too fast to be noticed. For diffusion limited response the approximating function [17,18] is given by:

$$\overline{\sigma(t)} = 1 - \frac{8}{\pi^2}e^{-t/\tau} - \frac{8}{9\pi^2}e^{-9t/\tau} - \frac{8}{25\pi^2}e^{-25t/\tau} - \cdots \tag{6}$$

with the time constant, τ:

$$\tau = \frac{4a^2}{\tilde{D}\cdot\pi^2} \tag{7}$$

a is the half thickness of the sample (diffusion length). The fit resulted in a value for τ of 78 h (2.8×10^5 s).

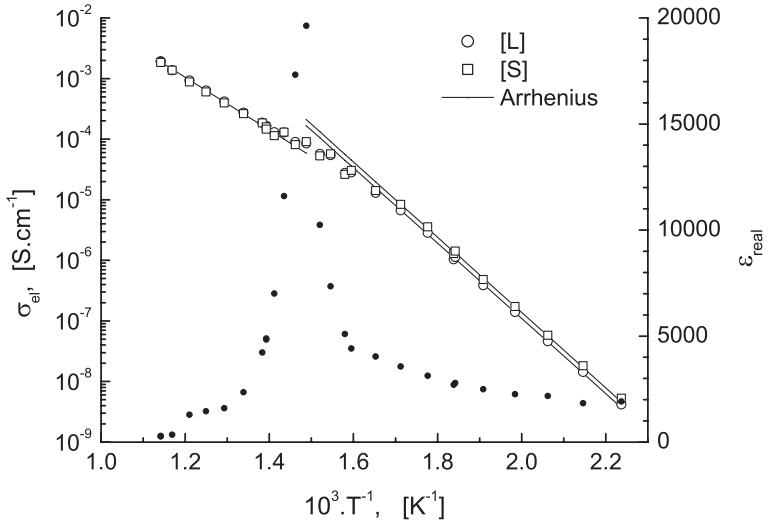

Fig. 6. Arrhenius graph of the electronic conductivity. (○) large sample, (□) small sample. The dielectric constant (●) is given for comparison (right hand axis). Lines represent the low- and high temperature models. Activation energies are presented in Table 2.

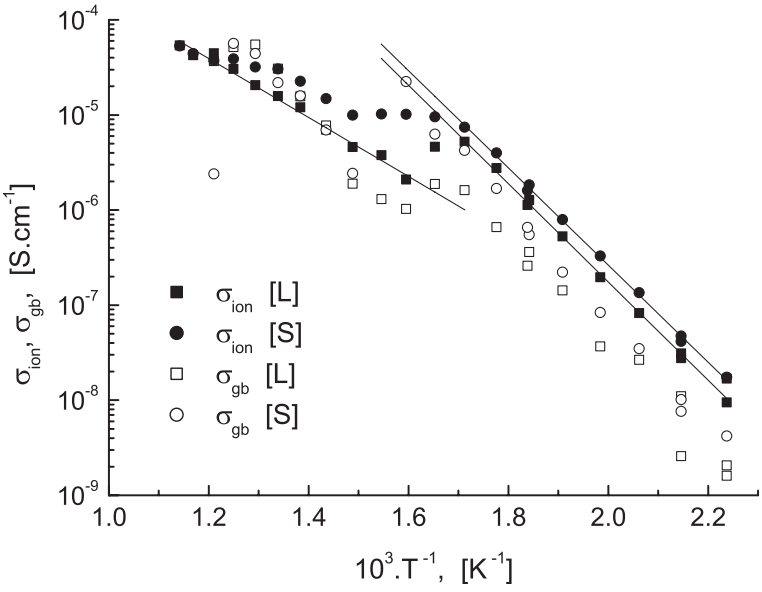

Fig. 7. Arrhenius graph of the apparent ionic (■,●) and grain boundary (□,○) conductivity. Squares: large sample; circles: smalls ample. Lines represent the low- and high temperature models for the data. Activation energies are presented in Table 2.

Substituting for the diffusion length, a, the radius of the sample a *chemical* diffusion coefficient of 2.3×10^{-7} $cm^2 \cdot s^{-1}$ is found. This is of course an approximate value as the geometry is not simply planar. Nor may it be expected that diffusion proceeds only through the cylindrical wall of the pellet. For the thin pellet the response, Eq. (5), could be modeled with a set of two (uncorrelated) time constants. The solid line through the open circles in Fig. 8 presents the model fit. The largest time constant of 81 h is identical to the time constant for the large sample. The smaller time constant is about 18.5 h, which can be tentatively related to the short diffusion path perpendicular to the flat surfaces.

Further impedance decay experiments with P_{O_2} steps to higher partial pressures at this temperature showed time constants in the order of 70–100 h. Hence the chemical diffusion coefficient seems to be fairly constant in this P_{O_2} range. In this extended time experiment the estimated P_{O_2} dependence for the electronic conductivity tended again to 1/4 as observed at 603 °C. The ionic conductivity remained virtually constant within the experimental error.

Table 2
Tabulation of activation energies for the electronic and ionic conductivity

	Temperature range [°C]	Activation energy [$kJ \cdot mol^{-1}$]
$\sigma_{electronic}$, air	200–320	119
$\sigma_{electronic}$, air	475–605	83
$\sigma_{electronic}$, N_2	200–425	105 ± 3
$\sigma_{electronic}$, N_2	530–630	89 ± 2
σ_{ionic}, air	200–320	98.5 ± 1
σ_{ionic}, air	440–605	60 ± 5
σ_{ionic}, N_2	100–385	114 ± 3
σ_{ionic}, N_2	425–630	28–40, [L]–[S]

4.6. Conductivity in N_2 rapidly cooled from 600 °C

The P_{O_2} dependence of the conductivity was checked once again at 603 °C. No deviations were observed. The samples were held at about 1.1 Pa of oxygen (nitrogen only) for a day to equilibrate. Next the conductivity cell was removed from the furnace and allowed to cool to room temperature under nitrogen atmosphere. The P_{O_2} remained at 1.1 ± 0.1 Pa during the cool down and following measurements. The conductivity was measured under N_2 from 22 °C up to 630 °C. Most of the spectra could be resolved with the extended circuit of Fig. 2C. At lower temperatures only part of the circuit could be applied due to limitations in the frequency range. Above about 375 °C the Randles type electrode response could be modeled with a pure capacitance and a Warburg, at lower temperatures more CPE-type behavior was observed for both elements.

4.7. Electronic conductivity in N_2

The electronic conductivity is presented in Fig. 9 together with σ_{el} measured in air. A significant decrease in σ_{el} is observed for the low temperature range. Again a transition from low-T Arrhenius type to high temperature Arrhenius behavior is observed around the Curie transition. Activation energies are quite close to those measured in air (Table 2).

4.8. Ionic conductivity in N_2

The ionic conductivities extracted from the data using the equivalent circuit of Fig. 2C presents again a very coherent pattern in Fig. 10. The ionic and grain boundary conductivities are quite close below the Curie transition. Above this transition the ionic conductivity presents a much lower

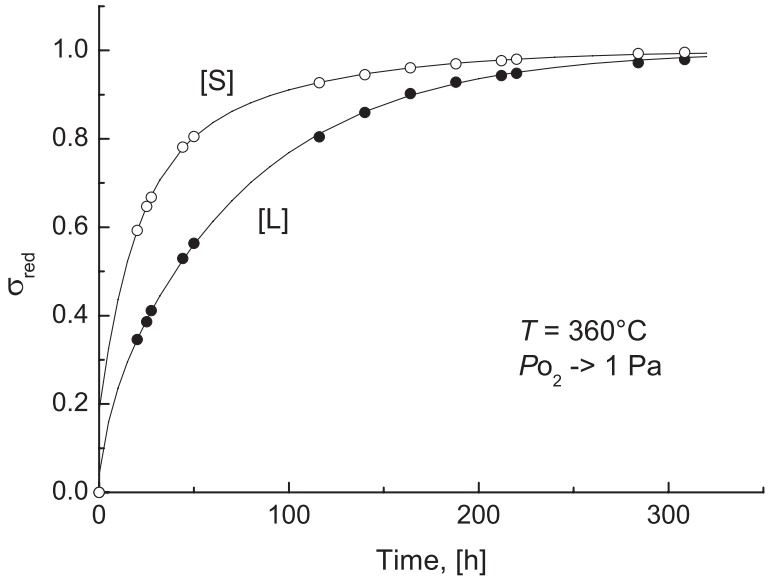

Fig. 8. Response of the electronic conductivity on a P_{O_2} jump from 20 kPa to 1 Pa. (●) large sample, (○) small sample. Solid lines are fitted to the data points; see text.

activation energy than σ_{gb}. It is quite remarkable that the small and large samples give almost identical results. Activation energies are tabulated in Table 2.

Fig. 11 clearly shows that the ionic conductivities above the Curie transition are almost independent of the P_{O_2}, as is in concordance with the P_{O_2} dependent measurements at 603 °C presented in Fig. 5. Below the transition a significant drop is observed, but this is probably for a large part due to the 'non-equilibrium' condition of the samples after the rapid cool down in N_2 atmosphere. This will be discussed further in Discussion.

4.9. Electrode response under N_2

Despite the complexity of the equivalent circuit of Fig. 2C the extracted parameters of the ionic electrode response present a clear picture as function of temperature, with relatively little scatter above the Curie transition. When corrected for the sample geometry, the obtained electrode parameters are quite close for both samples. For a true electrode process, however, one would rather expect these values to be independent of the thickness. This unexpected result will be discussed below.

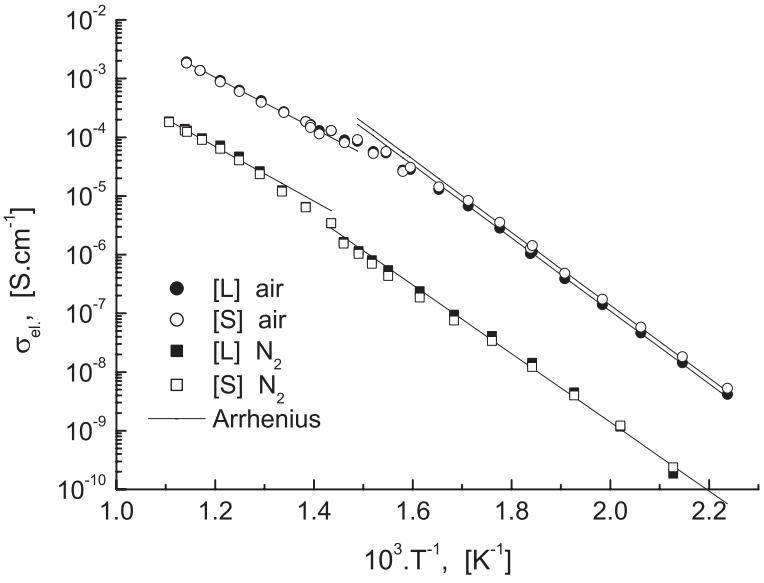

Fig. 9. Arrhenius graph of the electronic conductivity, measured after rapid cool down in N_2 from 603 °C (■,□). The electronic conductivity, as measured in air, is shown for comparison (●,○). Large sample: closed symbols, small sample: open symbols. Lines represent the low- and high temperature models. Activation energies are presented in Table 2.

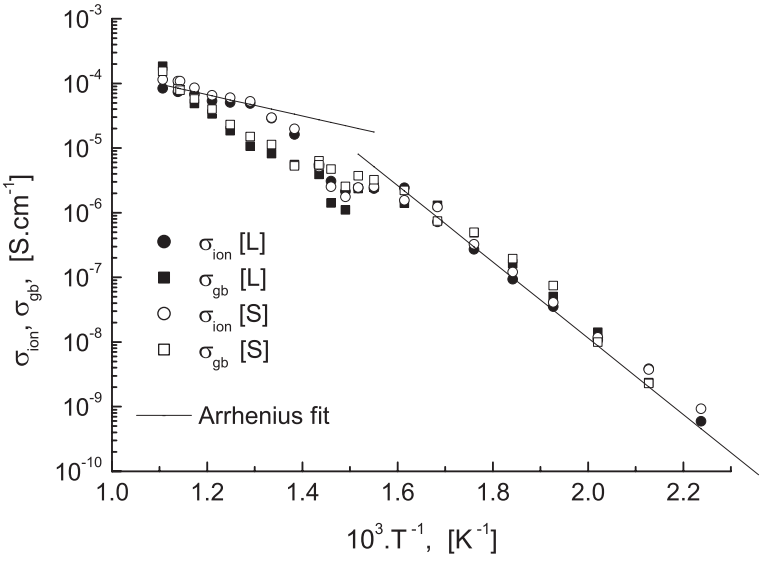

Fig. 10. Arrhenius plot of the ionic conductivity and the grain boundary conductivity in a N_2 atmosphere ($P_{O_2} \sim 1.1$ Pa).

Fig. 12 presents the double layer capacitance, C_{dl}, and the Warburg diffusion term, W_{diff}. The double layer capacitance shows moderate temperature dependence above the Curie transition. Below this transition it can be characterized as a moderately activated process with $E_{act} \sim 20$ kJ·mol^{-1}. The Warburg diffusion is quite distinct above the Curie transition. It can be observed in the impedance plot as a minute tail with $\sim 45°$ slope at the low frequency end. Below the Curie transition the parameter estimates become unreliable and show severe scatter.

The charge transfer resistance, however, can be followed to quite low temperatures and seems to present a clear Arrhenius behavior, excluding the transition temperature range. In Fig. 13 R_{ct} is presented as conductance. The small sample displays considerably more scatter than the large sample, for which a large activation energy is found: 106 kJ·mol^{-1}.

5. Discussion

5.1. Data analysis

The equivalent circuit (EqC) approach in the analysis of impedance spectra is not without controversy. Finding the 'optimum fit' without regard of a physical interpretation is, of course, not a sensible path to follow. Also an analysis that requires a large number of parameters, e.g. more than eight

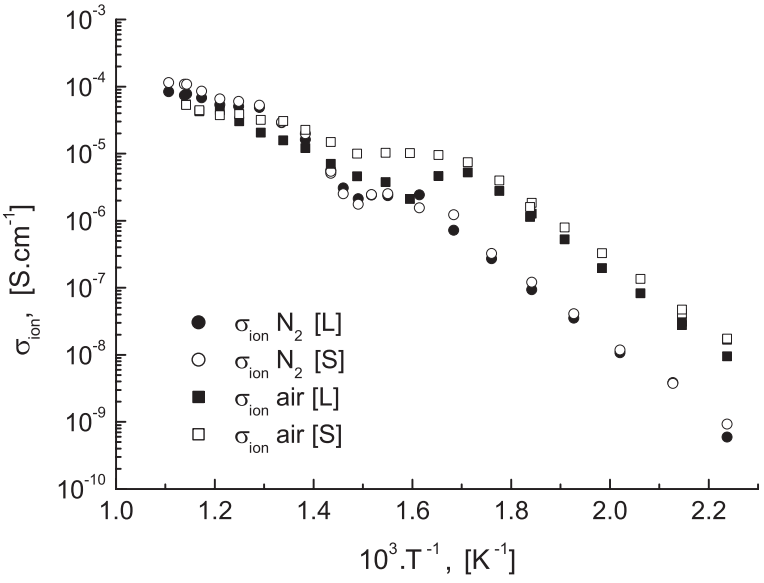

Fig. 11. Comparison of the ionic conductivities in air ($P_{O_2} \sim 20$ kPa) and in N_2 ($P_{O_2} \sim 1.1$ Pa) for the large and small sample. Conductivities above the Curie transition are identical within the experimental error limit.

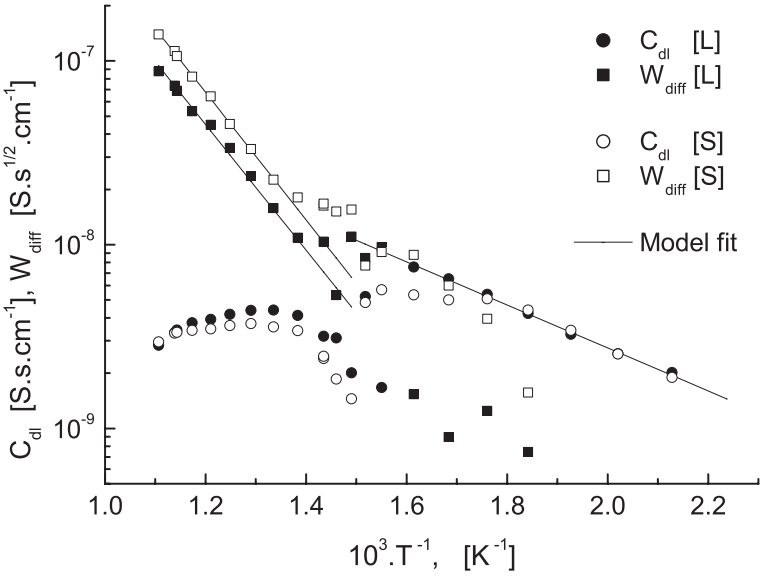

Fig. 12. Arrhenius presentation of the double layer capacitance, C_{dl}, and the diffusion Warburg, W_{diff}, which are associated with the ionic electrode response. Ambient is N_2 ($P_{O_2} \sim 1.1$ Pa). Above the Curie transition the Warburg is clearly activated with $E_{Act} = 65 \pm 3$ kJ.mol^{-1}. The parameters have been scaled by the geometric factor of the samples.

or nine, is often regarded with suspicion. The often-heard argument then is: with enough parameters 'one can fit an elephant'. But contrary to arbitrary fitting procedures using an extended set of polynomials, the response functions used in an equivalent circuit impose considerable restrictions on the modeling of the overall dispersion. Over-parameterization in the EqC-CNLS approach generally will lead to parameters set either to zero or infinity, or these will be accompanied by unrealistically large error estimates. In the extreme case one can use a very large number of dispersive sub-circuits (e.g. $R(RQ)_1 \ldots (RQ)_n$), which will generally give a reasonable to good fit, but without any physical meaning. This multi-(RQ) or -(RC) fit, on the other hand, is very useful in showing to what extend the data set is Kramers-Kronig transformable [13,19,20].

In fact, this Kramers-Kronig check should be the first step in the CNLS data analysis procedure. It will indicate systematic errors in the data due to, e.g. non-equilibrium conditions, non-linear response, slowly drifting temperature, continuing aging or degradation of the cell. The residuals

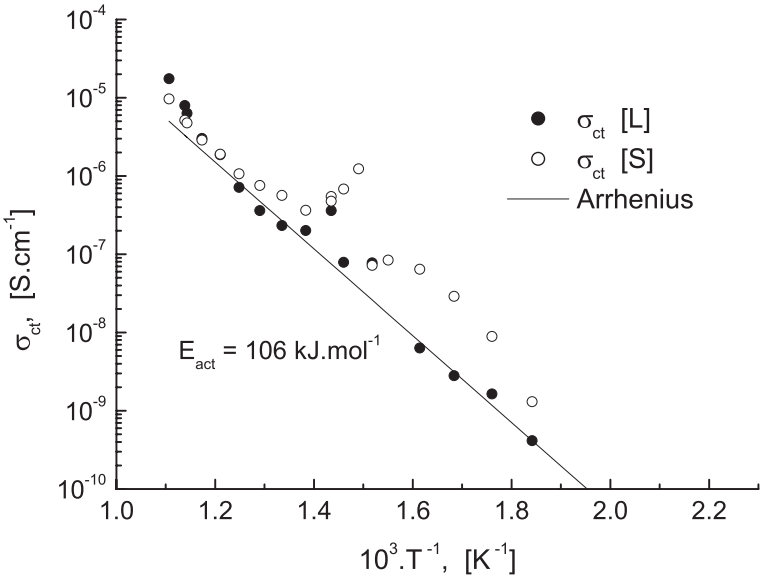

Fig. 13. Arrhenius plot of the charge transfer resistance, presented as conductance. Ambient is N_2 ($P_{O_2} \sim 1.1$ Pa). The parameters have been scaled by the geometric factor of the samples. The R_{ct} for the large sample shows activation over a temperature range extending below the Curie transition.

plot of the relative differences between the data and its Kramers-Kronig transform can be a very helpful tool in the subsequent CNLS-procedure, as it can be directly compared with the CNLS residuals [13].

A second important step is the 'pre-analysis' of the data, in which an appropriate equivalent circuit is constructed together with adequate starting values for the adjustable parameters in the overall CNLS-procedure. The pre-analysis technique is based on deconvolution by subtraction of recognizable dispersions, using a CNLS-fit of simple sub-circuits over a limited frequency range [14,21]. The power of this technique is that small but significant contributions to the overall dispersion can be detected. The deconvolution sequence presented in Fig. 3 clearly shows the advantages of this method.

Finally, the parameters obtained from the CNLS-procedure should present a consistent pattern as function of temperature and partial pressure. This is the ultimate test for a multi-parameter CNLS-procedure. But even then, one should realize that different EqC's might yield exactly, or within the experimental error, the same dispersion. Fletcher has presented an extensive tabulation of these 'degenerate circuits' [22]. Hence, the physical interpretation should be decisive in the selection of the most appropriate EqC. The equivalent circuits presented in Fig. 2 represent a physical interpretation with a direct electronic path (no electrode effects) and a 'blocked' ionic path, which over an extended temperature range also show specific electrode dispersion (Randles type circuit). The analysis leads to a consistent pattern as is evident from the Arrhenius graphs in Figs. 6 and 7, Figs. 9–13 and the P_{O_2} dependence in Fig. 5.

5.2. Mixed conduction and electrode response

An important warning must be issued in the special case of mixed (ionic and electronic) conductors. Although the ionic and electronic path may be obtained separately from the impedance spectra, the electrode dispersion involves both mobile species, as has been discussed in detail by Jamnik et al. [23,24]. This is due to the fact that any voltage difference between the electrodes will lead to a gradient in the oxygen activity [11]. Hence the non-stoichiometry parameter δ (as in $PbZr_{0.53}Ti_{0.47}O_{3-\delta}$) will be position dependent. This redistribution involves diffusion effects that will change from semi-infinite or Warburg-type diffusion for high frequencies to finite length diffusion (FLW) for (ultra) low frequencies.

A partially blocking electrode, e.g. porous Pt or Ag, can compound the problem by providing an extra current path by acting as oxygen electrode. Thus, the choice of electrode materials is crucial for impedance measurements on mixed conducting oxides. Dense gold electrodes have been proven to be the best choice, due to the relative inertness with respect to the adsorptive dissociation of gas phase oxygen [10–12]. One should be aware, however, that the mixed conducting oxide might also present catalytic properties towards the exchange reaction with ambient oxygen [25,26].

A good starting point for the analysis of the electrode dispersion is Eq. (9) in the publication by Jamnik and Maier [23], i.e. for the case of completely blocked ionic carriers:

$$Z(\omega) = R_\infty + \frac{(R_e - R_\infty)\tanh\sqrt{\frac{j\omega L^2}{4\tilde{D}}}}{\sqrt{\frac{j\omega L^2}{4\tilde{D}}} + j\omega(R_e + R_i)\frac{1}{2}C_{dl}\tanh\sqrt{\frac{j\omega L^2}{4\tilde{D}}}} \tag{8}$$

with:

$$R_\infty = \frac{R_e \cdot R_i}{R_e + R_i} \tag{9}$$

A slightly different nomenclature with respect to Ref. [23] is used here. This equation can be rearranged to:

$$\begin{aligned} Z(\omega) &= \frac{R_e}{R_e + R_i} \\ &\quad \times \left[R_i + \frac{R_e}{\sqrt{\frac{j\omega L^2}{4\tilde{D}}}\coth\sqrt{\frac{j\omega L^2}{4\tilde{D}}} + j\omega(R_e + R_i)\frac{1}{2}C_{dl}} \right] \\ &= \frac{R_e[R_i \cdot Q(\omega) + R_e]}{(R_e + R_i)\cdot Q(\omega)} \end{aligned} \tag{10}$$

with $Q(\omega)$ defined by:

$$Q(\omega) = \sqrt{\frac{j\omega L^2}{4\tilde{D}}}\coth\sqrt{\frac{j\omega L^2}{4\tilde{D}}} + j\omega(R_e + R_i)\frac{1}{2}C_{dl} \tag{11}$$

The complete dispersion of the combined ionic and electronic conduction process is presented in Fig. 14A. The dielectric response is not included in the simulation. It is easy to show that for $\omega \to 0$, Eq. (10) will reduce to $Z(\omega) = R_e$.

The data analysis shows that the electronic contribution is easily determined and subtracted, revealing the ionic path. The same can be done with Eq. (10):

$$\begin{aligned} &Z_{ion}(\omega) \\ &= R_i + \frac{1}{\frac{1}{R_e + R_i}\left[\sqrt{\frac{j\omega L^2}{4\tilde{D}}}\coth\sqrt{\frac{j\omega L^2}{4\tilde{D}}} - 1\right] + +j\frac{1}{2}\omega\cdot C_{dl}} \end{aligned} \tag{12}$$

The high frequency limit of $Z_{ion}(\omega)$ is, as expected, equal to R_i. The dispersion of Eq. (12) is presented in Fig. 14B. When $\omega \gg 4\tilde{D}/L^2$, then the coth() function will go to 1 and the vertical part of the electrode dispersion in Fig. 14B will

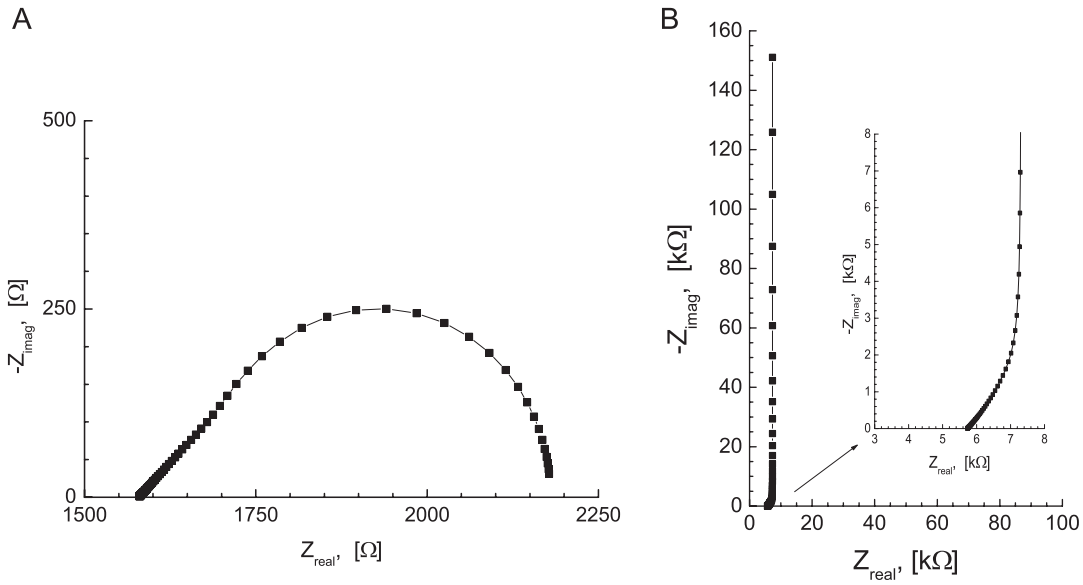

Fig. 14. Simulation of the electrode dispersion of a mixed conductor with ionically blocking electrodes, according to Eq. (12). Resistance values are taken from Table 1. Frequency range is 0.1 Hz to 10 kHz. $\tilde{D}=10^{-2}$ cm^2·s^{-1}. (A) Impedance presentation excluding the dielectric response. (B) Ibid., but with the electronic contribution subtracted. The inset is an enlargement of the high frequency range.

not be reached. This seems to be predominantly the case in the spectra obtained in this study. But further analysis indicates that $\omega \ll 4\tilde{D}/L^2$ must be reached in order to observe the 'dc-point' of the electronic conductivity in the full Eq. (8). This requires in combination with the measured ionic and electronic resistances and lowest frequency used, according to the model, unrealistically large diffusion coefficients in the order of 10^{-2} cm^2·s^{-1}.

A more direct analysis of the ionic path, using a simple diffusion–insertion model, can provide an estimate of the oxygen diffusion coefficient. Interactions with the electronic path are thus ignored. Based on the basic diffusion equations and boundary conditions the interface impedance, $Z_{\mathrm{int}}(\omega)$, can be presented as [11]:

$$Z_{\mathrm{int}}(\omega) = \frac{RTW}{4F^2c^0A}\,\frac{\tanh\sqrt{\dfrac{j\omega L^2}{4\tilde{D}}}}{\sqrt{j\omega\tilde{D}}} \qquad (13)$$

where W is the thermodynamic enhancement factor, $W = \mathrm{d}\ln a/\mathrm{d}\ln c$, c^0 is the concentration of (mobile) oxygen ions and A is the electrode area (cm^2). For $\omega \gg 4\tilde{D}/L^2$ (which is the case for $\tilde{D} \ll 2\times10^{-3}$ cm^2.s^{-1} for the small sample, a condition easily met in this investigation) this expression reduces to a semi-infinite diffusion (Warburg) expression:

$$Z_{\mathrm{int}}(\omega) = \frac{RTW}{4F^2c^0A\sqrt{j\omega\tilde{D}}} \qquad (14)$$

Unfortunately no data is available for the thermodynamic enhancement factor, but a value for D_{O} can be obtained from the partial ionic conductivity. For the measurement at 580 °C in N_2 (Fig. 3 and Table 1) this yields: $D_{\mathrm{O}} \approx 1.1\times10^{-5}$ cm^2·s^{-1}. Inserting the value of $W_{\mathrm{diff}} - Y_0$ from Table 1 into Eq. (14) yields for the ratio $\sqrt{\tilde{D}}/W \approx 8.6\times10^{-1/2}$cm s$^{-1/2}$. Combination results either in an extremely low value for $\tilde{D}$ or in an extremely high value for the thermodynamic enhancement factor, W. Hence, based on the two closely related analysis, the conclusion must be that the electrode response is not caused by bulk redox- and diffusion processes. A possible explanation could be a true oxygen electrode activity at the perimeter of the gold electrode, and possibly with contributions from pinholes within the electrode structure. The positive side is that the occurrence of a 'charge transfer resistance' can be explained with this interpretation. But it also requires a strong ionic blocking effect of the electrode.

5.3. Oxygen diffusion and P_{O_2} dependence of the conductivity

A much more direct estimate of the oxygen diffusion coefficients is found in the P_{O_2}-dependent measurements at 360 °C, Fig. 8. The excellent model-fits to the responses of both samples are quite surprising, especially the almost identical time constants for long times. That the small sample shows a different response type than the large sample can be explained by its much smaller thickness. This implies, however, that the electrodes are not completely dense, but probably covered with pinholes after the high temperature measurements. Thus a significantly shorter diffusion path is provided in the small sample, hence the separate 'short time' constant of 18.5 h, which is unrelated to the long time constant of 81 h.

Using the time constant of 78 h (2.8×10^5 s) of the large sample, the chemical diffusion coefficient, $\tilde{D}$, is estimated at 2.3×10^{-7} $cm^2 \cdot s^{-1}$. The ionic conductivity, including the grain boundary conductivity, results in a component diffusion coefficient, $D_O = 7.9 \times 10^{-12}$ cm^2 s^{-1}, which yields for the thermodynamic enhancement factor a quite high value of $\sim 3 \times 10^4$, but in concordance with an imperceptible small change in the ionic conduction, and hence in the oxygen vacancy concentration, for a large step in the oxygen partial pressure. This diffusion process is a clear indication of ionic conductivity in the PZT material.

Thus, the measured P_{O_2}-dependence at 603 °C can be interpreted with confidence as a p-type electronic conductivity with approximately a 1/4 power dependence on the oxygen partial pressure, and a constant, nearly P_{O_2}-independent, ionic conductivity. This is completely in agreement with literature [5], but it is probably the first time that this is deduced from accurate impedance measurements. The basic neutrality condition of Eq. (2), with $[V_O^{\cdot\cdot}] \approx [V''_{Pb}] \gg h^{\cdot}$, effectively explains the observations in Fig. 5. The electronic conductivity is higher than the ionic conductivity because the hole-mobility is much larger than the mobility of the oxygen ions, or $\sim$ vacancies, despite the large difference in concentrations.

5.4. Equilibration with the ambient

It is important to recognize the different equilibration reactions and the temperature ranges in which these are active with respect to the time scale of the measurement sequence. Maier has recently presented a thorough discussion of this phenomenon [27]. At high temperature, possibly above 700–800 °C [5], the equilibration with the ambient PbO partial pressure is of importance as it controls both the lead and oxygen vacancy concentrations:

$$Pb_{Pb}^{\times} + O_O^{\times} \rightleftarrows V''_{Pb} + V_O^{\cdot\cdot} + PbO_g \qquad (15)$$

Samples used in the present investigation were sintered at 1150 °C for 2 h in $PbTiO_3$ powder, followed by cool down at 5°/min. Depending on the rate of equilibration at 1150 °C, the cooling rate determines at what temperature the equilibrium lead vacancy concentration is frozen in. As all samples have been processed in exactly the same manner, it is no surprise that they show identical conductivities at intermediate temperatures ($\sim$ 400–650 °C).

From the experimental results it is quite evident that from about $\sim$ 400 °C down the oxygen non-stoichiometry becomes frozen-in. The equilibration rate depends also on sample dimensions, hence it will be clear that in the temperature range where the equilibration rate and $[dT/dt]$ are comparable the 'freeze-in' temperatures will be slightly different for different size samples. This will result in a small but noticeable difference in the conductivities, about a factor of 1.25 for the electronic conductivity (Fig. 6) and a factor of $\sim$ 1.6 for the ionic conductivity (Fig. 7).

5.5. Ionic conductivity

Assuming that, besides the mentioned lead- and oxygen vacancies, no other large concentrations of defects exist, Eq. (2) then predicts the oxygen vacancy concentration to be independent of P_{O_2}, as long as the relation $[V_O^{\cdot\cdot}] \gg h^{\cdot}$ holds. Within the experimental error, this is true for the oxygen ion conductivity above the Curie transition. The high temperature ionic conductivity in the cubic phase can thus be described by an activated migration with $E_{act} \approx 30$–60 $kJ \cdot mol^{-1}$ (the low accuracy is a result of the limited frequency range, which leads to considerable differences in the estimation of σ_{ion}). In the low temperature tetragonal phase, however, the ionic conductivity is governed by a more complex mechanism. This is evident from comparison of the Arrhenius graphs of Figs. 7 and 10. The activation energies (Table 2) and the pre-exponential factors are higher than in the cubic phase. The higher activation energy can be ascribed tentatively to either vacancy ordering, a well-known effect in the ferrite and cobaltate based perovskites [28], or defect association [29,30], both of which reduce the concentration of mobile vacancies.

The equilibration at 603 °C in N_2 (1.1 ± 0.1 Pa O_2) and subsequent rapid cool-down has a surprising effect on the electronic and ionic conductivities in the tetragonal phase. Fig. 9 shows that the electronic conductivity has dropped by a factor of $\sim$ 100. But the ionic conductivity has also decreased by a factor of 10–15, Fig. 11. Again the conductivity values obtained from the CNLS-analysis for the large and small sample are virtually identical, which is a results of the rapid 'freeze-in' of the equilibrium defect concentrations in the high temperature phase.

A possible explanation of the observed decreases in the electronic and ionic conductivities can be presented by considering the following defect mechanism. We assume that, in the tetragonal phase, electron holes can be trapped by lead vacancies:

$$Pb_{Pb}^{\cdot} + V''_{Pb} \rightleftarrows Pb_{Pb}^{\times} + V'_{Pb}, \quad K_{trap} = \frac{[Pb_{Pb}^{\cdot}] \cdot [V''_{Pb}]}{[V''_{Pb}]} \qquad (16)$$

Furthermore oxygen vacancies are attracted by the oppositely charged lead vacancies, forming immobile neutral complexes:

$$V''_{Pb} + V_O^{\cdot\cdot} \rightleftarrows [V''_{Pb} - V_O^{\cdot\cdot}]^{\times}, \quad K_{ass} = \frac{[V_O^{\cdot\cdot}] \cdot [V''_{Pb}]}{[V''_{Pb} - V_O^{\cdot\cdot}]} \qquad (17)$$

The binding energy between a doubly charged lead vacancy and an oxygen vacancy will be significantly larger than between a singly charged lead vacancy, Eq. (16), and an oxygen vacancy. Hence, these $[V'_{Pb} - V_O^{\cdot\cdot}]$ associates are

not taken into consideration. Thus the oxygen vacancy concentration can be linked directly to the concentration of electron holes and thus to the electronic conductivity. The concentration of $Pb_{Pb}^{\bullet}$ centers has been reduced significantly by the equilibration in N_2 at 600 °C, and thus in the subsequent set of measurements in N_2 ambient. This explains at least qualitatively the decrease in the oxygen ion conductivity. A simple model, based on Eqs. (2), (16) and (17 leads to the following relation between the mobile oxygen vacancies and the concentration of $Pb_{Pb}^{\bullet}$ (electron holes):

$$[V_O^{\bullet\bullet}] = \sqrt{K_{ass}\cdot([V_{Pb}^{q}]_{total} - [V_O^{\bullet\bullet}])\cdot\left(1 + \frac{[Pb_{Pb}^{\bullet}]}{K_{trap}}\right)} \qquad (18)$$

where $[V_{Pb}^{q}]_{total}$ represents the total lead vacancy concentration, which has been fixed by the equilibrium PbO-pressure at the sintering temperature. q represents the possible charges of the lead vacancy and its complexes, $[V_{Pb}^{q}]_{total}$ is given by:

$$[V_{Pb}^{q}]_{total} = [V_{Pb}''] + [V_{Pb}'] + [V_{Pb}'' - V_O^{\bullet\bullet}] \qquad (19)$$

Under the condition that $[V_O^{\bullet\bullet}] < [V_{Pb}^{q}]_{total}$ and $[Pb_{Pb}^{\bullet}] > K_{trap}$, which actually translates into $[V_O^{\bullet\bullet}] = [V_{Pb}']$, Eq. (18) simplifies to:

$$[V_O^{\bullet\bullet}] = \sqrt{[Pb_{Pb}^{\bullet}]\cdot[V_{Pb}^{q}]_{total}\frac{K_{ass}}{K_{trap}}} \qquad (20)$$

From this relation we find that for a decrease by a factor of 100 in the concentration of electronic charge carriers, the concentration of ionic charge carriers will decrease by a factor of 10. Assuming that the corresponding mobilities are independent of concentration, this then indicates that a decrease in the ionic conductivity by a factor of 10 can be related to a decrease by a factor of 100 in the electronic conductivity, quite in reasonable agreement with the observations.

Further experiments on samples with controlled defect concentrations, $[V_{Pb}'']$ and $[V_O^{\bullet\bullet}]$, will be needed to verify this model. Nevertheless, the presented measurements and subsequent analysis show that electronic and ionic conductivity can be effectively suppressed by equilibration in N_2 (low P_{O_2}) above the Curie temperature followed by rapid cool-down. This is of importance for application of PZT in e.g. memory devices at normal operating temperatures (< 60 °C).

5.6. Grain boundary dispersion

The small dispersion, as presented in Fig. 3C is tentatively interpreted as a grain boundary impedance in the ionic conduction path. Both samples present nearly identical values for this 'grain boundary conductivity', Figs. 7 and 10. Comparing these two figures shows that this σ_{gb} is less affected by the different oxidation states of the sample, showing a decrease by about a factor of 5–6 after the change in the ambient from 20 kPa to 1.1 Pa O_2. It is generally accepted that the grain boundary impedance is caused by space charge layers at the interface between the grains. This space charge layer is less dependent on the concentration of the mobile defects. The temperature dependence of the grain boundary impedance also changes over the transition from the ferro-electric phase to the para-electric phase above the Curie temperature.

5.7. Use of different sample thicknesses

As mentioned in the experimental procedure section, the use of two samples with different thickness is very useful in determining which part of the dispersion depends on bulk properties. Results show above ~ 400 °C quite good agreement for the electronic conductivity with deviations in the order of 2.5–6%. At low temperatures a constant difference of about 25% is found for the measurements in air, but this could be attributed to different freeze-in temperature, as explained above. Also the ionic conductivities are almost identical above the Curie temperature (when the experimental error permits), but also for the, in N_2 ambient, rapidly cooled samples, as is obvious from Fig. 11. This clearly points, as expected, to bulk properties.

For electrode related responses, a less clear relation is observed. But that should be no surprise as it is far more difficult to create exactly identical electrodes on different samples. Hence, it must be assumed that the observed correlation with sample thickness is rather coincidental. Analysis of more samples with different sizes will show how large the statistical spread in electrode properties can be. Another advantage of the use of samples with different dimensions is that it also shows in which temperature range the equilibration with the ambient is lost.

6. Conclusions

PZT shows clearly ionic and electronic conductivity from ~ 150 °C up. The electronic conductivity is strongly dependent on the thermal history and the oxygen partial pressure at high temperatures. The defect model can be presented by a simple equilibrium between the PbO partial pressure and lead vacancies at high temperatures, probably above 900–1000 °C. The lead vacancies are compensated by oxygen vacancies and 'electron holes' located at the lead sites, leading to small polaron hopping conduction. The oxygen vacancies equilibrate with the ambient P_{O_2} down to approximately 380–350 °C, at lower temperatures the oxygen vacancy concentration becomes 'frozen in'.

When rapidly cooled from 600 °C in N_2 the electronic conductivity is decreased by a factor of 100 in the ferro-electric phase. The ionic conductivity is found to decrease by a factor of 10–15. This is tentatively explained by defect

association, i.e. formation of $[V''_{Pb} - V^{\cdot\cdot}_{O}]$ clusters and interaction of singly charged lead vacancies (hole traps).

Acknowledgements

Financial support for Mai Pham from the MESA^{+} Institute for Nanotechnology is gratefully acknowledged. Mrs. J.A.M. Vrielink is thanked for the XRF measurement and analysis.

References

[1] G.H. Haertling, J. Am. Ceram. Soc. 82 (1999) 797.
[2] N. Duan, J.E. ten Elshof, H. Verweij, G. Greuel, O. Dannapple, Appl. Phys. Lett. 77 (2000) 3263.
[3] M.T.M. Pham, B.A. Boukamp, H.J.M. Bouwmeester, D.H.A. Blank, in: M.Á. Alario-Franco, M. Greenblatt, G. Rohrer, M.S. Whittingham (Eds.), Proceedings of the Materials Research Society Symposium: 'Solid-State Chemistry of Inorganic Materials IV', Mat. Res. Soc., Warrendale (PA), 2003 pp. 109–114.
[4] M.V. Raymond, D.M. Smyth, J. Phys. Chem. Solids 57 (1996) 1507.
[5] V.V. Prisedsky, V.I. Shishkovsky, V.V. Klimov, Ferroelectrics 17 (1978) 465.
[6] K. Nonaka, M. Akiyama, T. Hagio, A. Takase, J. Eur. Ceram. Soc. 19 (1999) 1143.
[7] W.C. Las, P.D. Spagnol, M.A. Zaghete, M. Cilense, Ceram. Int. 27 (2001) 367.
[8] A. Peláiz Barranco, F. Calderón Piñar, O. Pérez Martínez, J. De Los Santos Guerra, I. González Carmenate, J. Eur. Ceram. Soc. 19 (1999) 2677.
[9] A. Peláiz Barranco, F. Calderón Piñar, O. Pérez Martínez, E. Torres García, A. Huanosta-Tera, Acta Mater. 49 (2001) 3289.
[10] S.P.S. Badwal, M.J. Bannister, M.J. Murray, J. Electroanal. Chem. 168 (1984) 363.
[11] B.A. Boukamp, J.J.M. Bouwmeester, Solid State Ionics 157 (2003) 29.
[12] B.A. Boukamp, T.P. Raming, A.J.A. Winnubst, H. Verweij, Solid State Ionics 158 (2003) 381.
[13] B.A. Boukamp, J. Electrochem. Soc. 142 (1995) 1885.
[14] B.A. Boukamp, Solid State Ionics 18–19 (1986) 136.
[15] B.A. Boukamp, Solid State Ionics 20 (1986) 31.
[16] K. Keizer, Thesis, University of Twente, The Netherlands, 1976, Ch. 2.
[17] M.W. den Otter, B.A. Boukamp, H.J.M. Bouwmeester, H. Verweij, J. Electrochem. Soc. 148 (2001) J1–J6.
[18] B.A. Boukamp, M.W. den Otter, H.J.M. Bouwmeester, J. Solid State Electrochem. (in press).
[19] P. Agarwal, M.E. Orazem, L.H. Garcia-Rubio, J. Electrochem. Soc. 139 (1992) 1917.
[20] P. Agarwal, O.C. Mighissi, M.E. Orazem, L.H. Garcia-Rubio, Corrosion 49 (1993) 278.
[21] B.A. Boukamp, Solid State Ionics (in press).
[22] S. Fletcher, J. Electrochem. Soc. 141 (1994) 1823.
[23] J. Jamnik, J. Maier, J. Electrochem. Soc. 146 (1999) 4183.
[24] J. Jamnik, J. Maier, S. Pejovnil, Electrochim. Acta 44 (1999) 4139.
[25] B.A. Boukamp, ACH-Models Chem. 137 (2000) 225.
[26] B.A. Boukamp, Solid State Ionics 135–137 (2000) 75.
[27] J. Maier, Phys. Chem. Chem. Phys. 5 (2003) 2164.
[28] H. Kruidhof, H.J.M. Bouwmeester, R.H.E. van Doorn, A.J. Burggraaf, Solid State Ionics 63/65 (1993) 816.
[29] R. Merkle, J. Maier, Phys. Chem. Chem. Phys. 5 (2003) 2297.
[30] M.O. Zacate, L. Minervini, D.J. Bradfield, R.W. Grimes, K.E. Sickafus, Solid State Ionics 128 (2000) 243.